A dynamic multi-scale model for transient radiative transfer calculations

Maxime Roger, Nicolas Crouseilles

A dynamic multi-scale model for transient radiative transfer calculations

M. Roger[a], N. Crouseilles[b]

[a]*Mechanical Engineering Department, Instituto Superior Técnico/IDMEC, Technical University of Lisbon, Av. Rovisco Pais, 1049-001 Lisboa, Portugal*
[b]*INRIA-Rennes Bretagne-Atlantique (IPSO Project) and Université de Rennes 1 (IRMAR), Campus de Beaulieu, 35042 Rennes Cedex, France*

Abstract

A dynamic multi-scale model which couples the transient radiative transfer equation (RTE) and the diffusion equation (DE) is proposed and validated. It is based on a domain decomposition method where the system is divided into a mesoscopic subdomain, where the RTE is solved, and a macroscopic subdomain where the DE is solved. A buffer zone is introduced between the mesoscopic and the macroscopic subdomains, as proposed by Degond and Jin in [1], where a coupled system of two equations, one at the mesoscopic and the other at the macroscopic scale, is solved. The DE and the RTE are coupled through the equations inside the buffer zone, instead of being coupled through a geometric interface like in standard domain decomposition methods. One main advantage is that no boundary or interface conditions are needed for the DE. The model is compared to Monte Carlo, finite volume and P1 solutions in one dimensional stationary and transient test cases, and presents promising results in terms of trade-off between accuracy and computational requirements.

Keywords:

transient radiative transfer, multi-scale model, finite volume method, diffusion equation, domain decomposition

1. Introduction

In the last decades, many research fields and applications such as combustion, optical tomography, atmospheric physics or solar energy processes paid more attention to thermal radiation, and various numerical methods have been developed to improve the efficiency of the radiative transfer calculations [2]. Almost all of these methods are

based on the radiative transfer equation (RTE) or the diffusion equation (DE). The RTE is a kinetic transport equation for the radiative intensity, defined at the mesoscopic scale, and which represents the most accurate model for thermal radiation. The DE is a macroscopic model, where the P1 and the diffusion approximations are assumed, which is much more easier to solve, but remains inaccurate in a lot of physical situations. At the mesoscopic scale, the quantities depends on the position, the direction and time, while at the macroscopic scale, the dependence on the direction is not taken into account.

Indeed, the P1 approximation requires that the intensity within the medium be nearly isotropic. Calculating the radiative transfer using the DE with the so-called P1 method gives acceptable results in highly scattering media, but displays some major drawbacks in zone where the near-isotropic assumption is not valid, or if the system has subdomain where the medium is not optically thick, or when surface emission dominates over medium emission [2]. Moreover, the definition of the boundary conditions for the DE is a complicated issue where one has to respect constraints which can be very restrictive in numerous applications. Accordingly, the DE fails to describe accurately the light propagation in the proximity of boundaries or sources. Solutions have been proposed to improve the P1 model, such as the high order PN-approximations [3] or the modified and improved differential approximation [4, 5], but it is still very complicated to treat the boundary conditions with good accuracy.

Methods based on the RTE have been implemented and developed over the years such as the finite volume methods (FVM) [6], the discrete ordinate methods (DOM) [7], or the Monte Carlo methods (MCM) [8]. These methods offer a better accuracy than the P1 method [2], but require a higher computational effort due to the high dimensionality of the RTE. In these methods based on the mesoscopic model, the computational requirement is generally increasing with the optical thickness which is the inverse of the Knudsen number in radiative transfer. Therefore, at large optical thicknesses when the regime is diffusive, a large part of the computational time is due to a part of the system that could be more efficiently described by the DE. In practice, methods such as the FVM or the DOM become inefficient in the diffusive regime since the numerical parameters must respect strong constraints for stability

reasons. Typically, in transient calculations, the time step Δt has to be of the order of the square of the mean free path (the inverse of the optical thickness), and the mesh size Δx has to be lower than the mean free path, which is very small in the diffusive regime. Concerning the Monte Carlo method, the number of scattering events to be randomly generated is very large in the diffusive regime and requires consequently an important computational effort. Moreover, convergence difficulties may occur if the Monte Carlo algorithm is not correctly optimized for thick media [9].

Consequently, it seems natural to try to solve each model wherever it is appropriate. In multi-scale problems, where one has to deal with diffusive and kinetic regimes, a solution is to couple the DE with the kinetic model using a domain decomposition method, in which the system is decomposed into a macroscopic and a mesoscopic sub-domains. Domain decomposition strategies matching kinetic and diffusion models have received a lot of attention in the last decade (see [10, 11, 12, 13]). In particular, it has been tested in various studies [14, 15, 16, 17] in radiative transfer which showed a significant improvement over the P1 method, especially close to the boundaries. However, such strategies have to face the delicate issue of finding the interface conditions at the boundary of two neighboring decomposed domains.

A solution to overcome these difficulties related to the interface treatment is to introduce a buffer zone in which both the macroscopic and the mesoscopic models are solved and coupled, as proposed by Degond and Jin in [1]. In this approach, the two domains overlap but the solution of the original RTE equation can be recovered as the sum of the solutions of the two equations. The coupling is then applied through the equations rather than the boundary conditions. In the buffer zone, a smooth transition function makes the equations degenerate at the end of the buffer zone, and therefore, no boundary conditions are needed. So, in addition to the cost reduction due to the fact that the RTE is solved only where it is necessary (as in standard domain decomposition approaches), the present transition model overcomes the technical difficulties related to the definition of the boundary conditions of the DE (at the interface with the mesoscopic subdomain or at the frontier of the domain). Note that Degond *et al.* have also extended this approach for coupling kinetics and hydrodynamics equations in [18, 19, 20, 21].

In the present work, a dynamic multi-scale model is developed for transient radiative transfer calculations which couples the RTE with the DE, and is validated on one dimensional test cases. The model is extended in order to be efficient when collimated irradiation is considered at the boundary of the system. The present paper is organized in two main parts: Section 2 presents the dynamic multi-scale model developed for the coupling between the RTE and the DE, and is illustrated in a one dimensional (1D) stationary test case. In section 3, the model is extended to collimated irradiation and applied to transient radiative transfer. The results are compared with solutions obtained by Monte Carlo, finite volume, and P1 methods.

2. Dynamic multi-scale model for coupling the RTE and the DE

2.1. From the RTE to the DE

The RTE in absorbing and scattering media can be written as:

$$\frac{1}{c}\frac{\partial I}{\partial t} + \boldsymbol{u} \cdot \boldsymbol{\nabla} I = \sigma_a I_b - (\sigma_a + \sigma_s)I + \sigma_s \langle pI \rangle \tag{1}$$

where the mesoscopic unknown $I = I(\boldsymbol{r}, \boldsymbol{u}, t)$ is the radiative intensity, $\sigma_a = \sigma_a(\boldsymbol{r})$ and $\sigma_s = \sigma_s(\boldsymbol{r})$ are the absorption and scattering coefficients, respectively, $p(\boldsymbol{r}, \boldsymbol{u}|\boldsymbol{u}')$ is the normalized scattering phase function depending on the incident direction $\boldsymbol{u}'$ and the scattered one $\boldsymbol{u}$, and $I_b = I_b(\boldsymbol{r}, t)$ is the blackbody intensity (all these quantities and coefficients depends on the radiation frequency). For clarity reason, the in-scattering term is denoted by $\sigma_s \langle p(\boldsymbol{r}, \boldsymbol{u}|\boldsymbol{u}')I(\boldsymbol{r}, \boldsymbol{u}', t) \rangle = \sigma_s \langle pI \rangle$ where the symbols $\langle \cdot \rangle$ represent the integral over the solid-angle space $\langle f \rangle = \int_{4\pi} f d\Omega$. The general boundary conditions for an opaque surface with arbitrary surface properties can be written as:

$$I_w(\boldsymbol{r_w}, \boldsymbol{u}, t) = \epsilon_w I_b(\boldsymbol{r_w}, t) + \int_{\boldsymbol{u}\cdot\boldsymbol{n}>0} \rho(\boldsymbol{r_w}, \boldsymbol{u}|\boldsymbol{u}')I(\boldsymbol{r_w}, \boldsymbol{u}', t)(\boldsymbol{u}' \cdot \boldsymbol{n})d\Omega' \tag{2}$$

where $\boldsymbol{r_w}$ is a position at the boundary of the system, $\boldsymbol{n}$ is the local inward surface normal, $\epsilon_w = \epsilon(\boldsymbol{r_w}, t)$ is the emissivity and ρ is the bidirectional reflection function.

If the RTE is integrated over the solid-angle space 4π, the following equation is obtained:

$$\frac{1}{c}\frac{\partial \Phi}{\partial t} + \boldsymbol{\nabla} \cdot \boldsymbol{q} = \sigma_a[4\pi I_b - \Phi], \tag{3}$$

4

where Φ is the incident radiation, also called the fluence rate [22], and is defined by $\Phi = \langle I \rangle$. $\boldsymbol{q}(\boldsymbol{r}, t)$ is the radiative heat flux defined by $\boldsymbol{q} = \langle I\boldsymbol{u} \rangle$. With the P1 approximation, the radiative intensity is assumed nearly-isotropic, and is expressed according to the first order of the spherical harmonic expansion:

$$I = \frac{\Phi}{4\pi} + \frac{3}{4\pi}\boldsymbol{q} \cdot \boldsymbol{u}. \tag{4}$$

If the RTE is multiplied by the direction $\boldsymbol{u}$ and integrated over the solid-angle space, it is obtained:

$$\frac{1}{c}\frac{\partial \boldsymbol{q}}{\partial t} + \boldsymbol{\nabla} \cdot \langle (\boldsymbol{u} \otimes \boldsymbol{u})\, I \rangle = -[\sigma_a + (1-g)\sigma_s]\boldsymbol{q}, \tag{5}$$

where $g = \langle p(\boldsymbol{u} \cdot \boldsymbol{u'})\boldsymbol{u} \cdot \boldsymbol{u'} \rangle$ is the anisotropy factor, and where it has been assumed that the phase function depends only on the cosine-angle between the incident and the scattered directions $p(\boldsymbol{u}|\boldsymbol{u'}) = p(\boldsymbol{u} \cdot \boldsymbol{u'})$. If the P1 approximation is assumed, the term $\boldsymbol{\nabla} \cdot \langle (\boldsymbol{u} \otimes \boldsymbol{u})I \rangle$ on the left hand side is equal to $(1/3)\boldsymbol{\nabla}\Phi$. If the diffusion approximation is also assumed $((1/c)\partial \boldsymbol{q}/\partial t \simeq 0)$, $\boldsymbol{q}$ can be written as

$$\boldsymbol{q} = -D\boldsymbol{\nabla}\Phi, \quad \text{with} \quad D = \frac{1}{3[\sigma_a + (1-g)\sigma_s]}. \tag{6}$$

The coefficient D is called the diffusion coefficient. Finally, the diffusion equation is obtained,

$$\frac{1}{c}\frac{\partial \Phi}{\partial t} - \boldsymbol{\nabla} \cdot \left[D\boldsymbol{\nabla}\Phi\right] = \sigma_a[4\pi I_b - \Phi], \tag{7}$$

where the macroscopic unknown is $\Phi = \Phi(\boldsymbol{r}, t)$.

The exact boundary condition of Eq. (2) cannot be applied for the DE since the radiative intensity depends on the direction $\boldsymbol{u}$. So approximate boundary conditions must be used. It has been shown in [23] that the most accurate boundary conditions for the diffusion equation are the Marshak's boundary conditions [24], widely used in the literature, which ensures the conservation of radiative energy at boundaries. The Marshak's boundary conditions can be expressed as:

$$\int_{\boldsymbol{u}\cdot\boldsymbol{n}>0} I_w(\boldsymbol{u} \cdot \boldsymbol{n})d\Omega = \int_{\boldsymbol{u}\cdot\boldsymbol{n}>0} \left[\frac{\Phi}{4\pi} + \frac{3}{4\pi}\boldsymbol{q} \cdot \boldsymbol{u}\right](\boldsymbol{u} \cdot \boldsymbol{n})d\Omega, \tag{8}$$

where I_w is the exact boundary condition at point $\boldsymbol{r_w}$ for the radiative intensity and $\boldsymbol{n}$ is the ingoing normal at the boundary point $\boldsymbol{r_w}$. As pointed by Liu *et al.* in [25], one important shortcoming of the Marshak boundary conditions is to overpredict the surface heat transfer characteristics.

2.2. Transition model between the radiative transfer equation and the diffusion equation

A new model to couple the diffusion equation with the RTE is proposed in this section. It is based on the idea of Degond and Jin [1] who propose to introduce a buffer zone between the mesoscopic and the macroscopic subdomain. In this buffer zone, both models are solved through a coupled system of two equations, one equation at the mesoscopic scale, the other at the macroscopic scale. In the remainder, the buffer zone is denoted by the subdomain $\mathcal{B}$ and will be located between a kinetic (or mesoscopic) subdomain $\mathcal{K}$ where the RTE will be solved, and a macroscopic subdomain $\mathcal{M}$ where the diffusion equation will be solved (see Fig. 1). The $P1$ and the diffusion approximations are assumed in the buffer and the macroscopic zones.

The model is based on the introduction of a smooth transition function $h(\boldsymbol{r}, t)$ which define the buffer zone:

$$\begin{cases} h(\boldsymbol{r}, t) = 1 & \text{for} \quad \boldsymbol{r} \in \mathcal{K}, \\ h(\boldsymbol{r}, t) \in [0, 1] & \text{for} \quad \boldsymbol{r} \in \mathcal{B}, \\ h(\boldsymbol{r}, t) = 0 & \text{for} \quad \boldsymbol{r} \in \mathcal{M}. \end{cases} \tag{9}$$

The choice of h in the buffer zone is arbitrary. In this study, as discussed in the following, this function is chosen linear for simplicity reason.

The transition model consists in decomposing the radiative intensity into two functions $I = I_{\mathcal{K}} + I_{\mathcal{M}}$ defined by $I_{\mathcal{K}} = hI$ and $I_{\mathcal{M}} = (1-h)I$. In summary, in the kinetic zone where $h(\boldsymbol{r}) = 1$, the radiation intensity is equal to $I_{\mathcal{K}}$, while in the macroscopic zone where the radiation model is the diffusion equation, I is equal to $I_{\mathcal{M}}$. The definition of the transition function $h(\boldsymbol{r})$ degenerates the value of $I_{\mathcal{M}}$ at the interface with the kinetic zone, and degenerates the value of $I_{\mathcal{K}}$ at the interface with the macroscopic zone.

Let us multiply the RTE by the function h,

$$\frac{h}{c}\frac{\partial I}{\partial t} + h\boldsymbol{u} \cdot \boldsymbol{\nabla} I_{\mathcal{K}} + h\boldsymbol{u} \cdot \boldsymbol{\nabla} I_{\mathcal{M}} = h\sigma_a I_b - (\sigma_a + \sigma_s)I_{\mathcal{K}} + \sigma_s\langle pI_{\mathcal{K}}\rangle. \tag{10}$$

After developments, the following transport equation for $I_{\mathcal{K}}$ is obtained:

$$\frac{1}{c}\frac{\partial I_{\mathcal{K}}}{\partial t} + h\boldsymbol{u} \cdot \boldsymbol{\nabla} I_{\mathcal{K}} + h\boldsymbol{u} \cdot \boldsymbol{\nabla} I_{\mathcal{M}} = h\sigma_a I_b - (\sigma_a + \sigma_s)I_{\mathcal{K}} + \sigma_s\langle pI_{\mathcal{K}}\rangle + \frac{I}{c}\frac{\partial h}{\partial t}. \tag{11}$$

6

Now, if we multiply the RTE by $(1-h)$, the transport equation for $I_\mathcal{M}$ is obtained:

$$\frac{1}{c}\frac{\partial I_\mathcal{M}}{\partial t} + (1-h)\boldsymbol{u}\cdot\boldsymbol{\nabla}I_\mathcal{M} + (1-h)\boldsymbol{u}\cdot\boldsymbol{\nabla}I_\mathcal{K} =$$
$$(1-h)\sigma_a I_b - (\sigma_a + \sigma_s)I_\mathcal{M} + \sigma_s\langle pI_\mathcal{M}\rangle - \frac{I}{c}\frac{\partial h}{\partial t}. \quad (12)$$

It is important to note that if $(I_\mathcal{K}, I_\mathcal{M})$ are solutions of (11)-(12) with the initial conditions

$$I_\mathcal{K}|_{t=0} = hI_0, \quad I_\mathcal{M}|_{t=0} = (1-h)I_0, \quad (13)$$

then $I = I_\mathcal{K} + I_\mathcal{M}$ is solution of Eq. (1) with the initial condition $I|_{t=0} = I_0$ and conversely. The definition of h imposes that Eq. (11) is posed only in the subdomain $\mathcal{K} \cup \mathcal{B}$ while Eq. (12) is posed only in the subdomain $\mathcal{M} \cup \mathcal{B}$. If the boundaries are located inside the kinetic zone $\mathcal{K}$, the boundary conditions are not subject to any constraints related to the diffusion approximation.

In the subdomain $\mathcal{M} \cup \mathcal{B}$, the P1 and the diffusion approximations are assumed, and the diffusion equation (7) is multiplied by $(1-h)$ in order to obtain the transport equation for $\Phi_\mathcal{M}$:

$$\frac{1}{c}\frac{\partial \Phi_\mathcal{M}}{\partial t} - (1-h)\boldsymbol{\nabla}\cdot\left[D\boldsymbol{\nabla}(\Phi_\mathcal{M} + \langle I_\mathcal{K}\rangle)\right] = \sigma_a[4\pi(1-h)I_b - \Phi_\mathcal{M}] - \frac{\Phi_\mathcal{M} + \langle I_\mathcal{K}\rangle}{c}\frac{\partial h}{\partial t}. (14)$$

Finally, the system of equations (11)-(14) must be solved in the buffer zone with $I = I_\mathcal{M} + I_\mathcal{K}$ and

$$I_\mathcal{M} = (1-h)\left[\frac{\Phi}{4\pi} - \frac{3}{4\pi}D\boldsymbol{\nabla}\Phi\cdot\boldsymbol{u}\right] = \frac{\Phi_\mathcal{M}}{4\pi} - \frac{3}{4\pi}(1-h)D\boldsymbol{\nabla}(\Phi_\mathcal{M} + \langle I_\mathcal{K}\rangle)\cdot\boldsymbol{u}. \quad (15)$$

The kinetic equation (11) and the macroscopic equation (14) are coupled in the buffer zone $\mathcal{B}$. The factor $(1-h)$ degenerates the value of $\Phi_\mathcal{M}$ to zero at the interface $\mathcal{B} \cap \mathcal{K}$ between the kinetic zone and the buffer zone, where $(1-h) = 0$. Consequently no boundary conditions are needed for $\Phi_\mathcal{M}$ at the interface $\mathcal{B} \cap \mathcal{K}$ and at the boundaries of the system if those are located inside the kinetic zone.

The coupling between Eqs. (11) and (14) in the buffer zone is carried out in this study by an explicit discretization of the transient term. Assuming that $I_\mathcal{K}$ and $\Phi_\mathcal{M}$ are known at time t^n, the time algorithm for the model (11)-(14) is

- advance Eq. (11) by an explicit Euler scheme

$$
\begin{aligned}
I_\mathcal{K}^{n+1} \;=\;& I_\mathcal{K}^n - c\Delta t h \boldsymbol{u} \cdot \boldsymbol{\nabla}(I_\mathcal{K}^n + I_\mathcal{M}^n) + c\Delta t h \sigma_a I_b^n - c\Delta t(\sigma_a + \sigma_s)I_\mathcal{K}^n + \\
& c\Delta t \sigma_s \langle p I_\mathcal{K}^n \rangle + \Delta t(I_\mathcal{K}^n + I_\mathcal{M}^n)\frac{\partial h}{\partial t}(t^n),
\end{aligned}
\tag{16}
$$

where $I_\mathcal{M}^n$ is defined through (15) in which $I_\mathcal{K}$ and $\Phi_\mathcal{M}$ are evaluated at time t^n.

- advance Eq. (14) by an explicit Euler scheme

$$
\begin{aligned}
\Phi_\mathcal{M}^{n+1} \;=\;& \Phi_\mathcal{M}^n + c\Delta t(1-h)\boldsymbol{\nabla} \cdot \big[D\boldsymbol{\nabla}(\Phi_\mathcal{M}^n + \langle I_\mathcal{K}^n \rangle) \big] \\
& + c\Delta t \sigma_a[4\pi(1-h)I_b - \Phi_\mathcal{M}^n] - \Delta t(\Phi_\mathcal{M}^n + \langle I_\mathcal{K}^n \rangle)\frac{\partial h}{\partial t}(t^n).
\end{aligned}
\tag{17}
$$

2.3. Alternate model

The system (11)-(14) is obtained by assuming the diffusion and the P1 approximations on the total radiation intensity inside the buffer zone. Another possibility would have been to assume these approximations only on $I_\mathcal{M}$ instead of I. Let us start from the equation for $\Phi_\mathcal{M} = \langle I_\mathcal{M} \rangle$ (obtained from Eq. (12) integrated over the solid-angle space):

$$
\frac{1}{c}\frac{\partial \Phi_\mathcal{M}}{\partial t} + (1-h)\boldsymbol{\nabla} \cdot \boldsymbol{q} = \sigma_a[4\pi(1-h)I_b - \Phi_\mathcal{M}] - \frac{\Phi}{c}\frac{\partial h}{\partial t},
\tag{18}
$$

and from the equation for $\boldsymbol{q}_\mathcal{M}$ (obtained from Eq. (12) multiplied by $\boldsymbol{u}$ and integrated over the solid-angle space):

$$
\frac{1}{c}\frac{\partial \boldsymbol{q}_\mathcal{M}}{\partial t} + (1-h)\boldsymbol{\nabla} \cdot \langle (\boldsymbol{u} \otimes \boldsymbol{u})I_\mathcal{M} \rangle + (1-h)\boldsymbol{\nabla} \cdot \langle (\boldsymbol{u} \otimes \boldsymbol{u})I_\mathcal{K} \rangle = -(\sigma_a + \sigma_s(1-g))\boldsymbol{q}_\mathcal{M} \\
- \frac{\boldsymbol{q}_\mathcal{K} + \boldsymbol{q}_\mathcal{M}}{c}\frac{\partial h}{\partial t}.
\tag{19}
$$

Assuming the diffusion and the P1 approximations on $I_\mathcal{M}$ leads to

$$
(1-h)\frac{\boldsymbol{\nabla}\Phi_\mathcal{M}}{3} + (1-h)\boldsymbol{\nabla} \cdot \langle (\boldsymbol{u} \otimes \boldsymbol{u})I_\mathcal{K} \rangle = -\Big(\sigma_a + \sigma_s(1-g) + \frac{1}{c}\frac{\partial h}{\partial t}\Big)\boldsymbol{q}_\mathcal{M} - \frac{\boldsymbol{q}_\mathcal{K}}{c}\frac{\partial h}{\partial t},
\tag{20}
$$

which gives after development the following expression of $\boldsymbol{q}_\mathcal{M}$

$$
\boldsymbol{q}_\mathcal{M} = -(1-h)D^*\boldsymbol{\nabla}\Phi_\mathcal{M} - (1-h)3D^*\boldsymbol{\nabla} \cdot \langle (\boldsymbol{u} \otimes \boldsymbol{u})I_\mathcal{K} \rangle + \frac{3D^*}{c}\frac{\partial h}{\partial t}\boldsymbol{q}_\mathcal{K},
\tag{21}
$$

with $D^* = \frac{1}{3}\big(\sigma_a + (1-g)\sigma_s + \frac{1}{c}\frac{\partial h}{\partial t}\big)^{-1}$. Introducing this expression in Eq. (18) leads to

$$
\begin{aligned}
\frac{1}{c}\frac{\partial \Phi_\mathcal{M}}{\partial t} - (1-h)\boldsymbol{\nabla} \cdot \big((1-h)\big[D^*\boldsymbol{\nabla}\Phi_\mathcal{M}\big]\big) \;=\;& \sigma_a[4\pi(1-h)I_b - \Phi_\mathcal{M}] - \frac{\Phi}{c}\frac{\partial h}{\partial t} \\
& + (1-h)\boldsymbol{\nabla} \cdot \big((1-h)\big[3D^*\boldsymbol{\nabla} \cdot (\langle \boldsymbol{u} \otimes \boldsymbol{u} \rangle I_\mathcal{K})\big]\big) \\
& - (1-h)\boldsymbol{\nabla} \cdot \Big[\Big(\frac{3D^*}{c}\frac{\partial h}{\partial t} + 1\Big)\boldsymbol{q}_\mathcal{K}\Big].
\end{aligned}
\tag{22}
$$

with $I_\mathcal{M} = \frac{\Phi_\mathcal{M}}{4\pi} - \frac{3}{4\pi}D\boldsymbol{\nabla}\Phi_\mathcal{M}\cdot\boldsymbol{u}$. Solving Eq. (22) instead of Eq. (14) inside the buffer zone is attractive since the diffusion and the P1 approximations are assumed only on $I_\mathcal{M}$ instead of I, and that $I_\mathcal{K}$ stays untouched. However, it remains more complicated than solving Eq. (14) because of the additional source terms on the left hand side, and the spatial derivative of the transition function which must be estimated through the terms of $\boldsymbol{\nabla}\cdot\big((1-h)\big[D^*\boldsymbol{\nabla}\Phi_\mathcal{M}\big)\big]$. In future work, the performance of this alternate model will be tested and compared to the present one.

2.4. Illustrative example

A simple stationary test case, a 1D slab filled with a gray absorbing and scattering medium at temperature $T_g = 300K$ between two black walls at temperature $T_w = 1000K$ is considered in order to illustrate the advantage of the proposed multi-scale approach. The absorption and scattering coefficients are constant in the slab, and the scattering phase function is isotropic. The slab width is equal to $\ell = 1m$. The optical thickness is estimated by $\tau = (\sigma_a + \sigma_s)\ell$ where σ_a and σ_s are in m^{-1} and the albedo is defined by $\omega = \frac{\sigma_s}{\sigma_a+\sigma_s}$.

In stationary radiative transfer, the system of Eqs. (11)-(14) is simplified to:

$$h\boldsymbol{u}\cdot\boldsymbol{\nabla}I_\mathcal{K} + h\boldsymbol{u}\cdot\boldsymbol{\nabla}I_\mathcal{M} = h\sigma_a I_b - (\sigma_a + \sigma_s)I_\mathcal{K} + \sigma_s\langle pI_\mathcal{K}\rangle, \tag{23}$$

$$-(1-h)\boldsymbol{\nabla}\cdot\big[D\boldsymbol{\nabla}\Phi_\mathcal{M}\big] = \sigma_a[4\pi(1-h)I_b - \Phi_\mathcal{M}] + (1-h)\boldsymbol{\nabla}\cdot\big[D\boldsymbol{\nabla}\langle I_\mathcal{K}\rangle\big], \tag{24}$$

with $I_\mathcal{M} = \frac{\Phi_\mathcal{M}}{4\pi} - \frac{3}{4\pi}\boldsymbol{u}\cdot\Big[(1-h)D\boldsymbol{\nabla}(\Phi_\mathcal{M} + \langle I_\mathcal{K}\rangle)\Big]$. In the following, results obtained with the proposed model, referred as the FVM-P1 method, are compared with the finite volume method (FVM) and the P1 method. In the FVM, a first-order step scheme is used for the transport terms. The radiative intensity is constant inside a control angle and inside a control volume. The grids are uniform in the physical and the solid angle space. The solution is calculated by the point-by-point iterations according to the direction that the radiation beams propagates, as proposed in [26]. The diffusion equation in the P1 method is solved by a finite volume method with a second order central differencing. A tridiagonal matrix system is obtained and inverted. The Marshak boundary conditions are used at the wall. Concerning the FVM-P1 method, the same numerical schemes as the FVM are applied for the mesoscopic zone, and the same as the P1 method are applied for the diffusion equation. In the buffer zone, a

simple iterative procedure is carried out for the coupling between the mesoscopic and the macroscopic equations. Ten iterations are needed for convergence in this case.

In this example, the criteria chosen to define the transition function h, and thus to locate the buffer zone, is the scattering optical thickness defined by $\tau_s = \int_0^{|x-x_w|} \sigma_s(\ell)d\ell$, where x_w is a point defined at the boundary of the system. In the slab of width equal to $1m$, $x_w = 0$ or $x_w = 1m$. When the scattering optical thickness is higher than the limit $\tau_s^{inf} = \int_0^{|x^{inf}-x_w|} \sigma_s(\ell)d\ell$, the diffusion approximation is assumed and the current point x is located in the buffer zone. When the scattering optical thickness is higher than the second limit $\tau_s^{sup} = \int_0^{|x^{sup}-x_w|} \sigma_s(\ell)d\ell$, then the current point x is located in the macroscopic zone. Note that in the test case considered, the scattering coefficient is constant in the domain, and $\tau_s^{inf} = \sigma_s|x^{inf} - x_w|$ and $\tau_s^{sup} = \sigma_s|x^{sup} - x_w|$. In the buffer zone, the transition function goes from 1 at the interface with the kinetic zone until 0 at the interface with the diffusive zone. The function is chosen linear:

$$
\begin{cases}
\quad h(x) = 1 & \text{for} \quad x \in \mathcal{K}, \\
h(x) = \dfrac{\tau_s(x) - \tau_s^{inf}}{\tau_s^{sup} - \tau_s^{inf}} & \text{for} \quad x \in \mathcal{B}, \\
\quad h(x) = 0 & \text{for} \quad x \in \mathcal{M}.
\end{cases}
\tag{25}
$$

This choice has been motivated by the future objective of extending the method to multidimensional cases since another transition function may create interpolation problems when three dimensional cases are considered.

In Fig. 2(a), results are presented for an optical thickness τ equal to 10 and an albedo ω equal to 0.5. A uniform mesh is used where the number of spatial grid points for the FVM-P1, the FVM, and the P1 method is $N_x = 200$, and the number of angular grid points for the FVM-P1 and the FVM is $N_\theta = 32$. In the FVM-P1 method, the buffer zone is defined by $\tau_s^{inf} = 0.01$, and $\tau_s^{sup} = 0.75$ (corresponding to $x^{inf} = 0.02m$ and $x^{sup} = 0.15m$ near the left face of the slab, and $x^{inf} = 0.98m$ and $x^{sup} = 0.85m$ near the right face of the slab). In summary, the diffusion equation is solved in almost all the domain, except close to the boundaries. It is well known that the P1 approximation does not perform well when surface emission dominates over medium emission [2], and consequently the P1 method fail to predict correctly the fluence rate Φ close to the boundaries, as observed in Fig. 2(a). The FVM-P1 method shows a significant improvement in comparison with the P1 method. The results are

10

very close to the FVM. Inside the buffer zone, the FVM-P1 solution moves away from the FVM one, and smoothly gets closer to the P1 results inside the macroscopic zone. The P1 and the FVM-P1 curves are merged in the center of the macroscopic zone. The accuracy of the FVM-P1 is much better than the P1 method, even if the diffusion equation is still solved in the major part of the domain, which shows the potential improvement that can be obtained from the multi-scale approach. It is worth noting that the location of the buffer zone is arbitrary, and that it is always possible to improve the accuracy of the results, changing the size and/or the location of the buffer zone by modifying the definition of the transition function. In Fig. 2(b), various results of the FVM-P1 method are displayed with different location of the buffer zone. As expected, as long as the size of the kinetic zone is increased (τ_s^{inf} is increased) the results get closer to the reference FVM.

3. Application to transient radiative transfer with collimated irradiation

Over the last years, short-pulse laser applications have increased the interest in transient radiative transfer with collimated irradiation [27]. In optical tomography applications, the propagation of a short-pulse laser into a biological tissue is analyzed in order to determine the optical properties of the tissue for the detection of inhomogeneities and tumors [28]. Various methods based on the RTE for calculating efficiently transient radiative transfer have been proposed over the last years [29, 30, 31, 32]. In such methods, boundary conditions must describe accurately the time resolved short-pulse laser, and the biological tissue displays the optical properties of an optically thick medium with a strong albedo [33]. As shown by Tarvainen *et al.* in [15] and by Gorpas *et al.* [17], coupling the RTE with the DE can be an efficient solution for these problems where the boundary conditions must be modeled at the mesoscopic scale, and the propagation media may be accurately described by the diffusive regime. In this section, the dynamic multi-scale model is adapted to transient radiative transfer with collimated irradiation. Results are presented for the classical 1D test case studied by various authors [34, 35, 36] of a slab submitted to a short-pulse laser irradiation on one of its face. The temporal pulse shape is a truncated Gaussian distribution. The boundary condition is expressed by the radiative intensity at point $x = 0$ in $W.m^{-2}.str^{-1}$

11

by

$$I(0, \mu_c, t) = I_0 \delta(\mu - \mu_c) \exp\left[-4 \ln 2 \left(\frac{t - t_c}{t_p} \right)^2 \right] \quad, \quad 0 < t < 2t_c, \qquad (26)$$

where I_0 is the maximum intensity of the pulse which occurs at $t = t_c = 3t_p$. For $t > 2t_c$, the face is free from irradiation i.e. $I(0, \mu, t > 2t_c) = 0$. The medium inside the slab is cold (emission is neglected), absorbing and scattering with an isotropic phase function. The absorbing and scattering coefficients are homogeneous in the medium. The irradiation is a pulse normal to the left face of the slab ($\mu_c = \boldsymbol{u_c . n} = 1$).

Results will be compared with Monte Carlo (MC) reference solutions obtained by an inverse MC algorithm detailed in [37], and with the FVM and the P1 methods.

3.1. Models for improving the collimated irradiation treatment

The collimated irradiation treatment can be efficiently improved by decomposing the radiative intensity $I = I_d + I_c$ into contributions from the collimated irradiation I_c, and contributions from the diffuse radiation I_d [31]. A photon is removed from the collimated contribution by absorption or scattering: after a first scattering event, a photon is transferred from the collimated part to the diffusive part. The collimated radiative intensity $I_c = I_c(\boldsymbol{r}, \boldsymbol{u}, t)$ obeys the following equation

$$\frac{1}{c} \frac{\partial I_c}{\partial t} + \boldsymbol{u} \cdot \boldsymbol{\nabla} I_c = -(\sigma_a + \sigma_s) I_c. \qquad (27)$$

On the other side, the transport equation for I_d writes

$$\frac{1}{c} \frac{\partial I_d}{\partial t} + \boldsymbol{u} \cdot \boldsymbol{\nabla} I_d = \sigma_a I_b - (\sigma_a + \sigma_s) I_d + \sigma_s \langle p I_d \rangle + \sigma_s \langle p I_c \rangle. \qquad (28)$$

The benefits of this separate treatment are a more accurate estimation of the transport of the short-laser pulse through the participating media [31]. In the remainder, the modified FVM solution is based on the discretization of Eq. (28), and on the integral formulation of I_c:

$$I_c(x, \mu, t) = I(0, \mu_c, t - x/(\mu_c c)) \exp\left(-\int_0^{x/\mu_c} (\sigma_a + \sigma_s) dl \right) \delta(\mu - \mu_c). \qquad (29)$$

Concerning the diffusion equation, following the approach outlined by Star [22] or Modest [2], the collimated irradiation treatment can be improved by the so-called

12

modified P1 approximation. Integration of Eq. (28) over the solid-angle space leads to the transport equation for Φ_d

$$\frac{1}{c}\frac{\partial \Phi_d}{\partial t} + \boldsymbol{\nabla} \cdot \boldsymbol{q_d} = -\sigma_a[\Phi_d - 4\pi I_b] + \sigma_s \Phi_c, \qquad (30)$$

where $\Phi_c = \langle I_c \rangle$. The modified P1 approximation consists in assuming the P1 and the diffusion approximations for I_d so that the diffuse radiative heat flux $\boldsymbol{q_d}$ is:

$$\boldsymbol{q_d} = -D\boldsymbol{\nabla}\Phi_d + \frac{\sigma_s g}{\sigma_t^*}\boldsymbol{q_c}, \qquad (31)$$

where $\sigma_t^* = \sigma_a + \sigma_s(1 - g)$ and $D = 1/(3\sigma_t^*)$. The following diffusion equation is obtained for the transport of the diffuse fluence rate Φ_d

$$\frac{1}{c}\frac{\partial \Phi_d}{\partial t} - \boldsymbol{\nabla} \cdot (D\boldsymbol{\nabla}\Phi_d) = -\sigma_a[\Phi_d - 4\pi I_b] + \sigma_s \Phi_c - \boldsymbol{\nabla} \cdot \left[\frac{\sigma_s g}{\sigma_t^*}\boldsymbol{q_c}\right]. \qquad (32)$$

In summary, in the modified $P1$ approximation, Eq. (27) is used to estimate I_c, from which we can compute $q_c = \langle \boldsymbol{u} I_c \rangle$ and Eq. (32) is solved for the estimation of Φ_d which enables to construct I_d thanks to $I_d = \frac{\Phi_d}{4\pi} + \frac{3}{4\pi}\boldsymbol{q_d} \cdot \boldsymbol{u}$.

An example of comparison between the classical and the modified methods is presented in Fig. 3. For the FVM, the modified FVM, the P1 and the modified P1 methods, the first order explicit time scheme is used to discretize the transient term and the upwind scheme is used for spatial derivative. A second order central differencing scheme is used for the second derivative in the diffusion equation. The number of spatial grid points is $N_x = 200$, and the number of angular grid points (for the classical and modified FVM) is $N_\theta = 32$. The time history transmittance T, which is defined by $T(t) = \frac{2\pi}{I_0} \int_0^1 I(x = 1, \mu, t)d\mu$, at the right face (defined by $x = 1m$) is displayed. A significant improvement of the accuracy is observed for the modified FVM and P1 methods in comparison with the classical ones. As expected, the classical P1 method is unable to predict correctly the variation of the transmittance with time. It is observed in Fig. 3 that the modified methods improves the accuracy of the short-pulse laser transport through the slab, as stated by Boulanger and Charette in [31].

Results obtained with the classical and the modified FVM converge towards the Monte Carlo solution when N_x is increased and the convergence of the FVM is much slower than the convergence of the modified FVM. It must be emphasized that the

upwind scheme (also called step scheme) is not appropriate for capturing strong time variation as shown by Chai in [35]. Therefore, results obtained with the classical and modified FVM may be improved with the use of a bounded higher order schemes such as the CLAM scheme [35]. The numerical strategy has been chosen very simple in this work (first order and second order numerical schemes have been used for spatial and time derivatives) in order to focus only on the efficiency and the advantages that can be gained from the proposed dynamic multi-scale model. In future work, numerical methods will be investigated in order to improve the efficiency of the present approach in more complex problems, such as multidimensional and/or heterogeneous medium.

3.2. Modified dynamic multi-scale model for collimated irradiation

Following the same methodology as in section 2.2, it is easy to extend the dynamic multi-scale model for collimated irradiation treatment. The diffusive component of the radiative intensity is decomposed into $I_d = I_\mathcal{K} + I_\mathcal{M}$, where $I_\mathcal{K} = hI_d$ and $I_\mathcal{M} = (1-h)I_d$. The radiative intensity, like in section 3.1, is decomposed into its collimated component and its diffuse component: $I = I_c + I_\mathcal{K} + I_\mathcal{M}$. Then the same developments as in section 2.2 are applied to Eq. (28). In a first stage, Eq. (28) is multiplied by h which leads to:

$$\frac{1}{c}\frac{\partial I_\mathcal{K}}{\partial t} + h\boldsymbol{u}\cdot\boldsymbol{\nabla}I_\mathcal{K} \; + \; h\boldsymbol{u}\cdot\boldsymbol{\nabla}I_\mathcal{M} =$$
$$h\sigma_a I_b - (\sigma_a + \sigma_s)I_\mathcal{K} + \sigma_s\langle pI_\mathcal{K}\rangle + h\sigma_s\langle pI_c\rangle + \frac{I_d}{c}\frac{\partial h}{\partial t}. \quad (33)$$

In a second stage, assuming the $P1$ approximation for I_d along with the diffusion approximation in the buffer and the diffusive zones, Eq. (32) can be multiplied by $(1-h)$ to obtain:

$$\frac{1}{c}\frac{\partial \Phi_\mathcal{M}}{\partial t} - (1-h)\boldsymbol{\nabla}\cdot(D\boldsymbol{\nabla}\Phi_d) \;=\; -\sigma_a[\Phi_\mathcal{M} - 4\pi(1-h)I_b] + (1-h)\sigma_s\Phi_c$$
$$-(1-h)\boldsymbol{\nabla}\cdot\left[\frac{\sigma_s g}{\sigma_t^*}\boldsymbol{q_c}\right] - \frac{\Phi_d}{c}\frac{\partial h}{\partial t}. \quad (34)$$

The system of equations (27)-(33)-(34), satisfied by $(I_c, I_\mathcal{K}, \Phi_\mathcal{M})$, is then solved. Integrating Eq. (33) over the solid-angle space and adding the obtained equation to Eq. (34) leads to Eq. (32). The present model (27)-(33)-(34) can then be viewed as an intermediate model between the modified P1 approximation given by (27)-(32) and the modified RTE model (27)-(28).

3.3. Application

In this section, the (modified) FVM-P1 method is compared with the (modified) FVM, the (modified) P1 and the Monte Carlo methods [1]. The same numerical strategy as described for the FVM and the P1 methods in section 3.1 has been applied for the discretization of Eqs. (27), (33) and (34) in the FVM-P1 method.

3.3.1. Definition of the dynamic transition function

In Fig. 3, it is observed that the diffusion approximation cannot predict correctly the short-pulse laser propagation through the slab. The modified model allows to predict correctly the photons that exit the system without scattering event, but it remains inaccurate for short-paths, *i.e.*, when the photons exit the system after a few scattering events. Therefore, at the initial instants, when the photons are transmitted after short optical paths, predictions made by the P1 method are inaccurate and the error is maintained at the following instants. So the strategy consists to solve the mesoscopic model at the first instants, and to solve the macroscopic model when the diffusion approximation can be assumed, when the photons exit the system after a large number of scattering events (after long optical paths). Two instants $t_i(x)$ and $t_f(x)$ are then defined at point x. Before the instant $t_i(x)$, the RTE is solved, and therefore the initial transition function $h_i(x)$ is equal to 1. After the second instant $t_f(x)$ the diffusion approximation is applied at point x and therefore the transition function vanishes (except for x close to the boundaries of the system). The final transition function $h_f(x)$ defined for $t > t_f(x)$ can be written as (if the left face of the slab is defined at $x = 0$ and the right face at $x = 1$):

$$
\begin{cases}
\quad h_f(x) = 1 & \text{if} & x \le d & \text{or} & (1-x) \le d, \\
\quad h_f(x) = (d + \Delta d - x)/\Delta d & \text{if} & d < x < d + \Delta d, \\
h_f(x) = (d + \Delta d - (1-x))/\Delta d & \text{if} & d < (1-x) < d + \Delta d, \\
\quad h_f(x) = 0 & \text{if} & x \ge d + \Delta d & \text{or} & (1-x) \ge d + \Delta d,
\end{cases}
\tag{35}
$$

where d represents the distance from the boundaries for which the interface between the buffer zone and the kinetic zone are defined, and Δd is the width of the buffer zone

---

[1]In the remainder of this section, the word modified will be skipped

$((d + \Delta d)$ denotes the distance from the boundaries for which the interface between the macroscopic and the buffer zones are defined). Fig. 4 displays the final transition function h_f with an illustration of the notations.

Between the instants $t_i(x)$ and $t_f(x)$ the time evolution of the transition function is assumed to be linear with respect to the time t:

$$h(x,t) = \frac{h_f(x) \times (t - t_i(x)) + h_i(x) \times (t_f(x) - t)}{t_f(x) - t_i(x)}. \tag{36}$$

3.3.2. Results

In Fig. 5, the time evolution of the transmittance is displayed for an optical thickness equal to 10, an albedo $\omega = 0.5$. The dimensionless time defined by $t_p^* = c(\sigma_a + \sigma_s)t_p$ is 0.5. The boundary conditions are given by Eq. 26. In the FVM-P1 method, the initial instant t_i has been fixed to $t_i(x) = 2t_c + (x/c)$. This choice guarantees that, first, all photons located at x at time $t_i(x)$ have already suffered at least one scattering event, and second, the major part of the photons emitted around the time t_c (when the radiation intensity amplitude is close to the maximum $I(0, \mu_c, t_c) = I_0$) have already experienced various scattering events. This choice ensures the validity of the diffusion approximation. The second instant $t_f(x)$ is chosen equal to $t_f(x) = t_i(x) + \Delta t$ where the time interval width is fixed to $\Delta t = 2t_c$. The distance d is chosen equal to zero (which means that the interface between the buffer zone and the kinetic zone is fixed at the boundary) and the size of the buffer zone is $\Delta d = 0.1$. As expected, the FVM-P1 method shows an important improvement of the results compared to the P1 method.

The difference observed between the FVM and the FVM-P1 solution in Fig. 5 can be controlled by increasing the time interval width Δt as shown in Fig. 6(a), and/or by increasing the time t_i such as in Fig. 6(b). Another possibility is to define the size of the buffer zone Δd according to the physical quantities needed. In optical tomography problem, the quantity to be defined is generally related to the incident radiation on a detector. It is then possible to define a bigger buffer zone close to the detector, and a thinner one close the others boundaries of the system. For instance, if the transmittance is needed, it is possible to increase the size of the buffer zone close to the right face of the slab, and to decrease it, and even deleting it, close to the left

face[2]. In this case, with $d = 0$, the final transition function $h_f(x)$ for $t > t_f(x)$ can be expressed as:

$$\begin{cases} h_f(x) = \frac{\Delta d - (1-x)}{\Delta d} & \text{for} \quad (1-x) < \Delta d, \\ h_f(x) = 0 & \text{for} \quad (1-x) \geq \Delta d. \end{cases} \tag{37}$$

The influence of Δd on the results is illustrated in Fig. 6(c).

Obviously, all these parameters t_i, Δt, or Δd must be defined according to the physical configuration. For instance, if the albedo ω is fixed to 0.9 (albedo which is frequently encountered in biomedical applications, see [27]), the diffusion approximation cannot be assumed at a time $t = 2t_c + \frac{x}{c}$ like in the case $\omega = 0.5$. Thus, the time t_i must be increased in order to obtain a good estimation of the FVM-P1 method, as shown in Fig. 7 where t_i has been fixed to $8t_c + \frac{x}{c}$.

In table 1, the CPU times are compared. The so-called "case 1" represents the simulations displayed in Figs. 5 and 6 (with $\omega = 0.5$), while "case 2" represents the simulations displayed in Fig. 7 (with $\omega = 0.9$). The time gained by the FVM-P1 over the FVM is more important in "case 1" because the *macroscopic* time interval, *i.e.* the time interval during which the macroscopic model is used, in the FVM-P1 method is larger than in "case 1": $t_f = 2t_c$ for "case 1" whereas $t_f = 10t_c$ for "case 2". Calculations have also been carried out for an increased number of angular grid points ($N_\theta = 64$). The difference between the FVM-P1 and the FVM becomes more significant. For instance, denoting by t_{P1} the CPU time of a P1 simulation in "case 1", the CPU time for the FVM is $6t_{P1}$ while the CPU time for the FVM-P1 is only $3.9t_{P1}$. This suggests that the benefit of using the FVM-P1 method must be more significant in multidimensional cases, where the number of discrete solid-angles is higher than in 1D cases.

4. Conclusion

A new multi-scale model for radiative transfer calculations has been developed and applied to stationary and transient 1D test cases. The model is based on a new strategy

---

[2]If the buffer zone disappears close to the left face, the boundary condition must be defined for the diffusion equation. For times t such that $t > t_i$, the influence of the boundary condition at the left face is no longer important and the Marshak boundary conditions can be used.

for coupling the RTE with the DE, which consists in introducing a buffer zone, in which two equations at two different scales (mesoscopic and macroscopic) are solved. This model couples the RTE and the DE through the equations in the buffer zone, whereas in standard domain decomposition methods the coupling is done through a geometric interface. One main advantage of the method is that it allows to avoid the complicated issue of defining interface conditions for the DE and the RTE.

The model has been discretized with a finite volume approach, and compared to Monte Carlo reference results, a FVM where only the RTE is solved, and a P1 method where only the DE is solved. The results obtained are promising. The smooth transition function is easy to handle and enables to couple the mesoscopic and the macroscopic equations in a very robust way. Like in classical domain decomposition method, it is possible to increase the size of the subdomain where the RTE is solved in order to improve the accuracy, or to decrease it in order to accelerate the calculations. Moreover, the proposed model enables to control in a simple way the RTE/DE coupling through the transition function, instead of controlling the coupling through complicated interface. The smooth transition function depends on time and allows a dynamic control of the size of the macroscopic and the kinetic zones. Therefore, the dynamic multi-scale model can offer an interesting alternative way to deal with complex geometry, compared to a standard decomposition method where the delicate issue of geometric interfaces has to be handled.

In future work, natural extensions to transient multidimensional cases will be explored. The numerical method and the definition of the transition function, which define the size of the different zone in the decomposition of the domain, will be investigated. In this study, the transition functions have been chosen according to parameters such as the scattering optical thickness, the pulse time-width, or the distance from the boundaries. In multidimensionnal problem, a transition function which depends on these parameters may be defined and applied in different configurations in order to provide a complete guideline for the application of the dynamic multi-scale model proposed. Further discussions about the choice of the transition function inside the buffer zone have also to be performed. They have been chosen linear for simplicity reasom in this work, but other smoother functions may be tested in order to determine if it is

possible to improve the trade-off between accuracy and computational requirements.

[1] P. Degond, S. Jin, A smooth transition model between kinetic and diffusion equations, SIAM J. Numer. Anal. 42 (2005) 2671–2687.

[2] M. Modest, Radiative heat transfer, New-York: McGraw-Hill, 2003.

[3] M. Modest, J. Yang, Elliptic pde formulation and boundary conditions of the spherical harmonics method of arbitrary order for general three-dimensional geometries, J. Quant. Spectrosc. Radiat. Transf. 109 (9) (2008) 1641–1666.

[4] M. Modest, J. Yang, The improved differential approximation for radiative heat transfer in multi-dimensional media, J. Heat Transf. 112 (1990) 819–821.

[5] M. Ravishankar, S. Mazumder, M. Sankar, Application of the modified differential approximation for radiative transfer to arbitrary geometry, J. Quant. Spectrosc. Radiat. Transf. 111 (2010) 2052–2069.

[6] J. Chai, S. Patankar, Finite volume method for radiation heat transfer, Adv. Heat Transf. 2 (2000) 110–135.

[7] W. Fiveland, Discrete-ordiantes solutions of the radiative transport equation for rectangular enclosures, J. Heat Transf. 106 (1984) 699–706.

[8] J. Howell, The Monte Carlo method in radiative heat transfer, J. Heat Transf. 120 (3) (1998) 547–560.

[9] V. Eymet, R. Fournier, S. Blanco, J. Dufresne, A boundary based net exchange Monte Carlo method for absorbing and scattering thick media, J. Quant. Spectrosc Radiat. Transf. 91 (2003) 27–46.

[10] G. Bal, Y. Maday, Coupling of transport and diffusion models in linear transport theory, Math. Modeling and Numer. Anal. 36 (2002) 69–86.

[11] F. Golse, S. Jin, C. Levermore, A domain decomposition analysis for a two-scale linear transport problem, Math. Model. Num. Anal. 37 (2003) 869–892.

[12] X. Yang, F. Golse, Z. Huang, S. Jin, Numerical study of a domain decomposition method for a two-scale linear transport equation, Networks and Heterogeneous Media 1 (2006) 143–166.

[13] M. Tidriri, New models for the solution of intermediate regimes in transport theory and radiative transfer: existence theory, positivity, asymptotic analysis, and approximations, J. Stat. Phys. 104 (2001) 291–325.

[14] A. Klar, N. Siedow, Boundary layers and domain decomposition for radiative heat transfer and diffusion equations: applications to glass manufacturing process, European J. Appl. Math. 9 (2) (1998) 351–372.

[15] T. Tarvainen, M. Vauhkonen, V. Kolehmainen, S. Arridge, J. Kaipio, Coupled radiative transfer equation and diffusion approximation model for photon migration in turbid medium with low-scattering and non-scattering regions, Phys. Med. Biol. 50 (2005) 4913–4930.

[16] J. Densmore, T. Urbatsch, T. Evans, M. Buksas, A hybrid transport-diffusion method for Monte Carlo radiative-transfer simulations, J. Comput. Phys. 222 (2007) 485–503.

[17] D. Gorpas, D. Yova, K. Politopoulos, A three-dimensional finite elements approach for the coupled radiative transfer equation and diffusion approximation modeling in fluorescence inaging, J. Quant. Spectrosc. Radiat. Transf. 111 (2010) 553–568.

[18] P. Degond, S. Jin, L. Mieussens, A smooth transition model between kinetic and hydrodynamic equations, J. Comput. Phys. 209 (2005) 665–694.

[19] P. Degond, J. Liu, L. Mieussens, Macroscopic fluid models with localized kinetic upscaling effects, Multiscale Model. Simul. 5 (3) (2006) 940–979.

[20] P. Degond, G. Dimarco, L. Mieussens, A moving interface method for dynamic kinetic-fluid coupling, J. Comput. Phys. 227 (2007) 1176–1208.

[21] P. Degond, G. Dimarco, L. Mieussens, A multiscale kinetic-fluid solver with dynamic localization of kinetic effects, J. Comput. Phys. 229 (2010) 4907–4933.

[22] W. Star, Optical-thermal response of laser-irradiated tissue, chapter 6 : Diffusion Theory of Light Transport, Plenum, New York, 1995.

[23] B. Davison, Neutron Transport Theory, Clarendon Press, Oxford, 1958.

[24] R. Marshak, Note on the spherical harmonics method as applied to a milne problem for a sphere, Physical Review 71 (7) (1947) 443–446.

[25] F. Liu, J. Swithenbank, E. Garbett, The boundary condition of the p_n-approximation used to solve the radiative transfer equation, Int. J. Heat Mass Transf. 35 (8) (1992) 2043–2052.

[26] W. Fiveland, Three-dimensional radiative heat-transfer solutions by the discrete-ordinates method, J. Thermophysics 2 (4) (1988) 309–316.

[27] S. Kumar, K. Mitra, Microscale aspects of thermal radiation transport and laser application, Adv Heat Transfer 33 (1999) 187–294.

[28] S. Wan, Z. Guo, S. Kumar, J. Aber, B. Garetz, Noninvasive detection of inhomogeneities in turbid media with time-resolved log-slope analysis, J. Quant. Spectrosc. Radiat. Transf. 84 (2004) 493–500.

[29] Z. Guo, K. Kim, Ultrafast-laser-radiation transfer in heterogeneous tissues with the discrete-ordinate method, Appl. Opt. 42 (2003) 2897–2905.

[30] J. Chai, P. f Hsu, Y. Lam, Three dimensional transient radiative transfer modeling using the finite-volume method, J. Quant. Spectrosc. Radiat. Transf. 86 (2004) 299–313.

[31] J. Boulanger, A. Charette, Numerical developments for short-pulsed near infra-red laser spectroscopy. part i: direct treatment, J. Quant. Spectrosc. Radiat. Transf. 91 (2005) 189–209.

[32] S. Mishra, P. Chugh, P. Kumar, K. Mitra, Development and comparison of the DTM, the DOM and the FVM formulations for the short-pulse laser transport through a participating medium, Int. J. Heat Mass Transf. 49 (2006) 1820–1832.

[33] Z. Guo, S. Wan, K. Kim, C. Kosaraju, Comparing diffusion approximation with radiation transfer analysis for light transport in tissues, Optical Review 10 (5) (2003) 415–421.

[34] C.-Y. Wu, Propagation of scattered radiation in a participating planar medium with pulse irradiation, J. Quant. Spectrosc. Radiat. Transf. 64 (2000) 537–548.

[35] J. Chai, Finite volume method for transient radiative transfer, Numerical Heat Transf., Part B 44 (2003) 187–208.

[36] L. Ruan, S. Wang, H. Qi, D. Wang, Analysis of the characteristics of time-resolved signals for transient radiative transfer in scattering participating media, J. Quant. Spectrosc. Radiat. Transf. 111 (2010) 2405–2414.

[37] M. Roger, Modèles de sensibilité dans le cadre de la méthode de Monte-Carlo : Illustrations en transfert radiatif, Ph.D. thesis, INP Toulouse, France (2006). URL http://ethesis.inp-toulouse.fr/archive/00000317/

	$\dfrac{t_{FVM-P1}}{t_{P1}}$	$\dfrac{t_{FVM}}{t_{P1}}$
case 1, $N_\theta = 32$	2.7	3.4
case 1, $N_\theta = 64$	3.9	6.0
case 2, $N_\theta = 32$	3.1	3.4
case 2, $N_\theta = 64$	4.9	6.2

Table 1: Comparison of the CPU times of the FVM-P1 and the FVM simulations relative to the CPU time of the P1 method (t_{p_1}). The "case 1" represents the simulations displayed in Figs. 5 and 6, whereas "case 2" corresponds to the simulations displayed in Fig. 7.
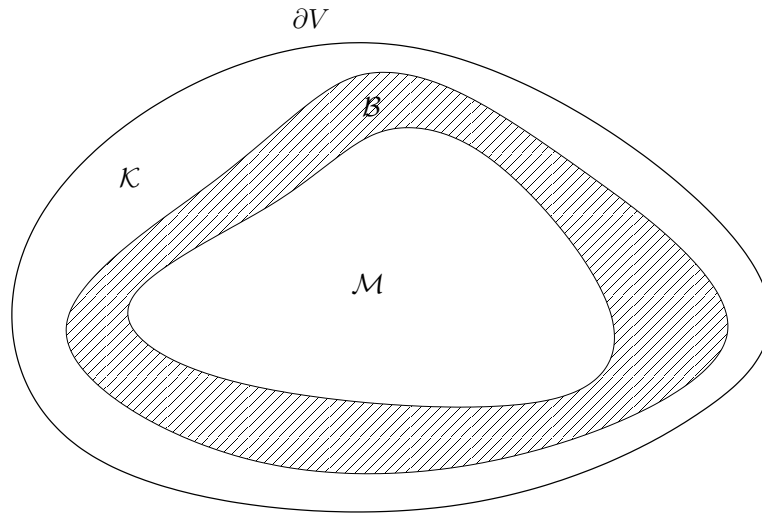
Figure 1: Scheme of the decomposition domain method with the introduction of the buffer zone $\mathcal{B}$. The kinetic subdomain is denoted by $\mathcal{K}$ while the macroscopic subdomain is denoted by $\mathcal{M}$.
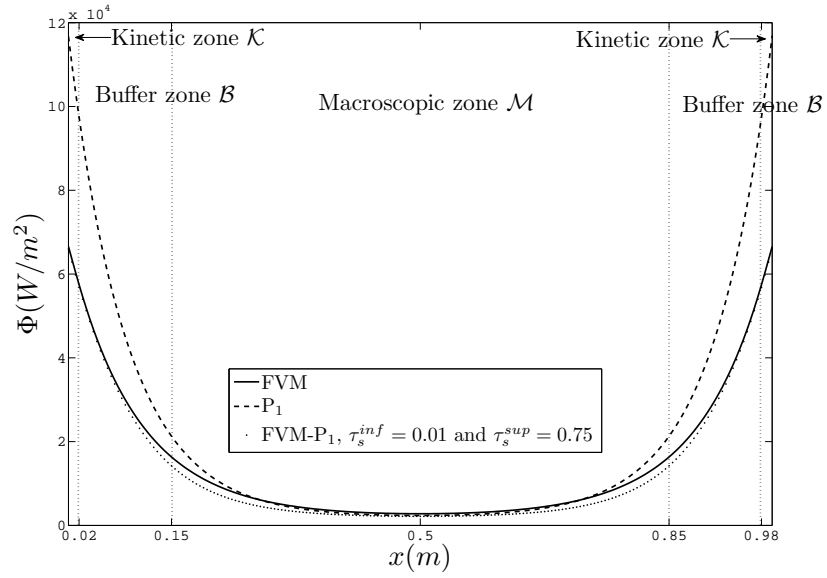
(a)
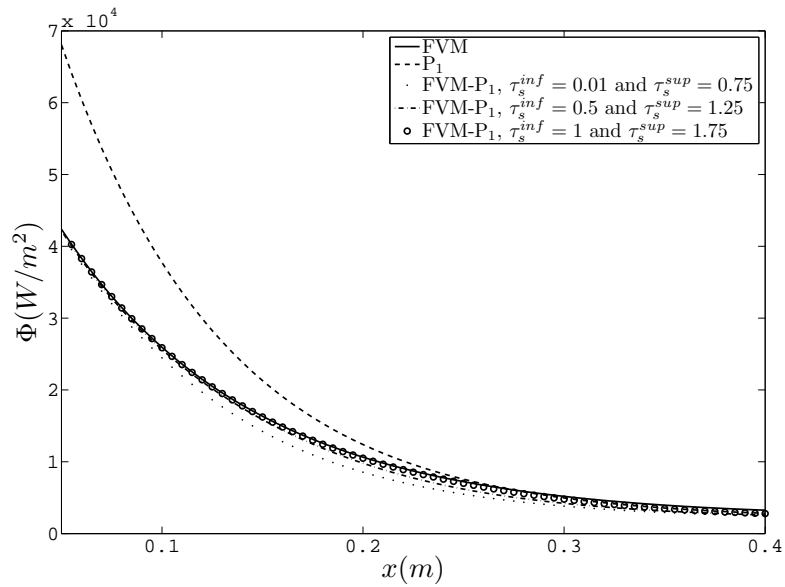
(b)

Figure 2: Comparison of the fluence rate estimated by the FVM-P1, the FVM, and the P1 methods, as a function of the spatial direction. In Fig. (b), the FVM-P1 solutions are given for different locations of the buffer zone.
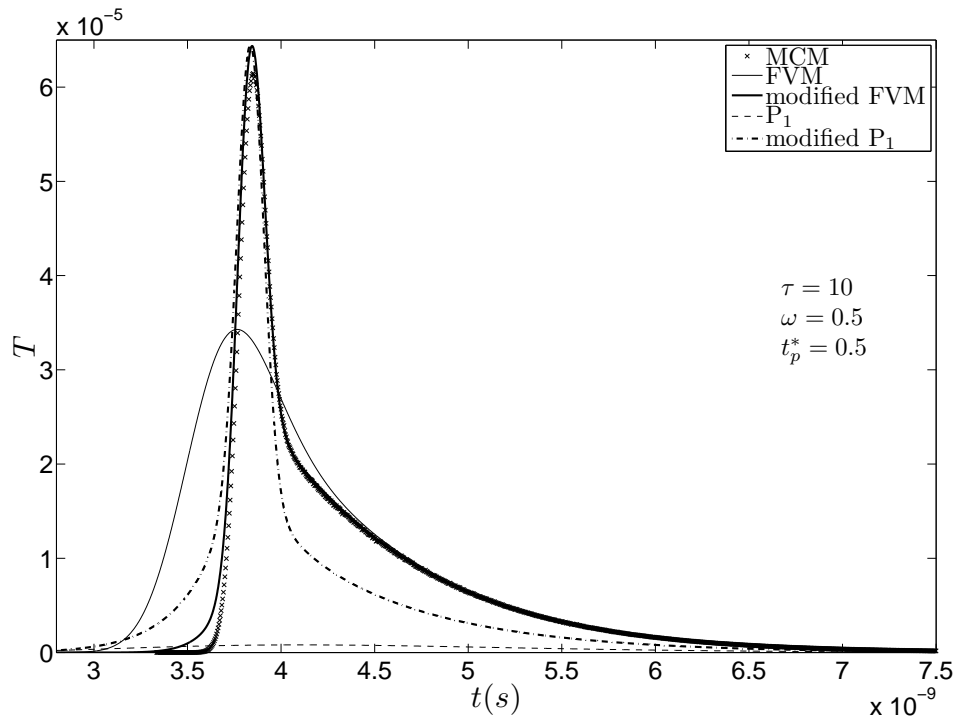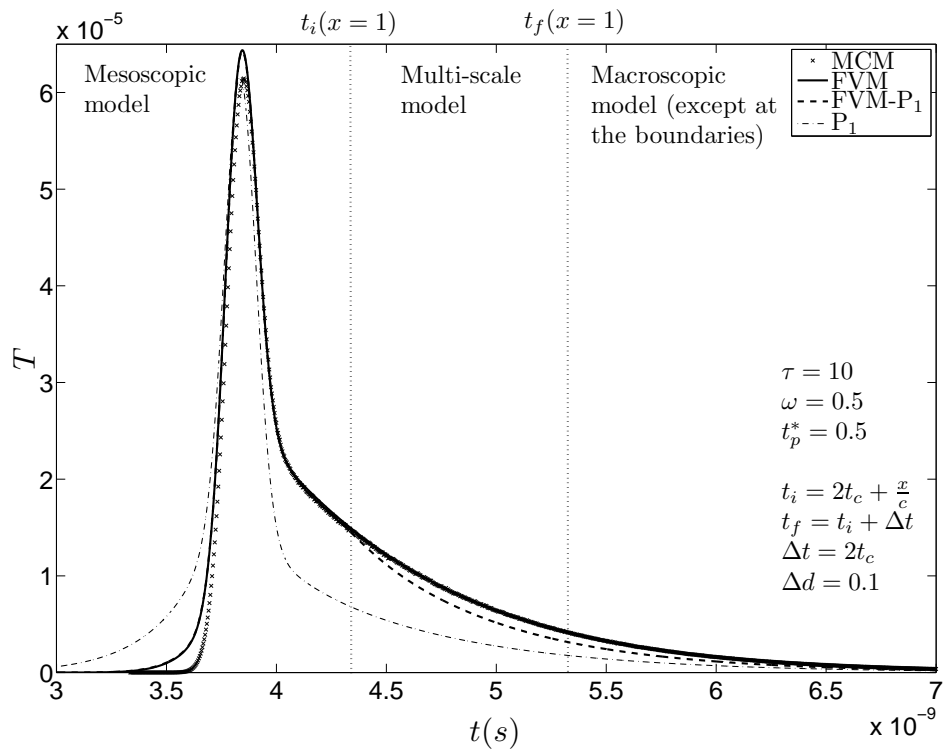
Figure 3: Time history of the transmittance: comparison between Monte Carlo solution, classical and modified model for the FVM and the P1 methods. t_p^* is the dimensionless time defined by $t_p^* = c(\sigma_a + \sigma_s)t_p$.
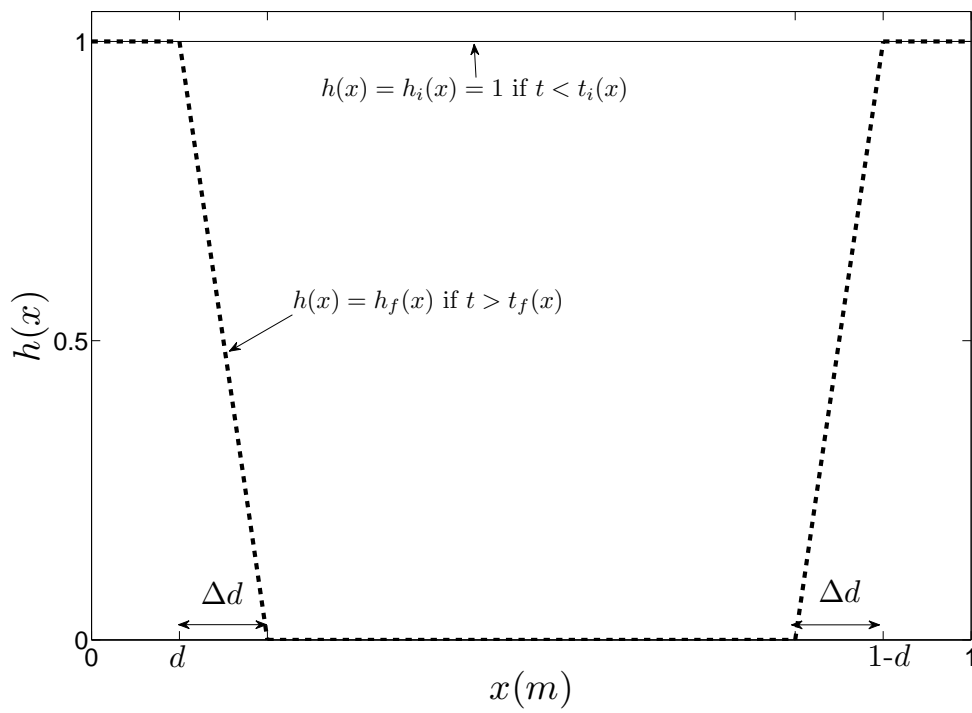
Figure 4: Scheme of h_i (transition function at time $t_i(x)$) and of h_f (transition function at time $t_f(x)$), as a function of the spatial variable.
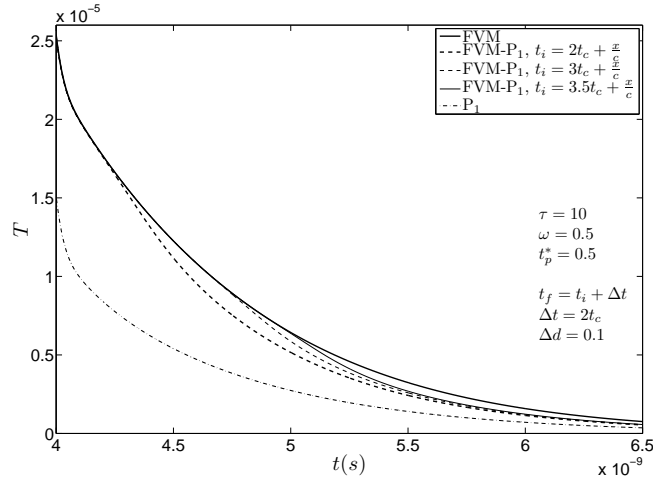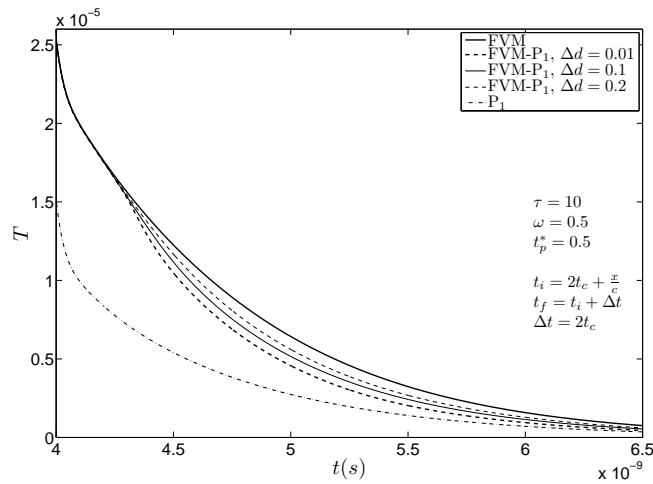
Figure 5: Time history of the transmittance: comparison between the Monte Carlo, FVM-P1, FVM, and P1 methods. The time interval width Δt is fixed to $2t_c$ in the FVM-P1 method.
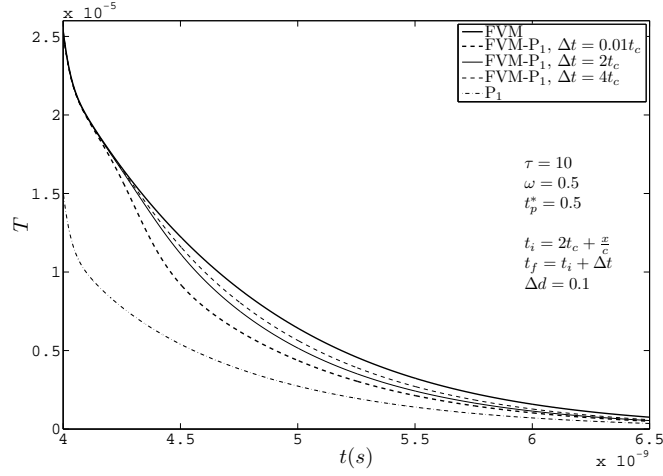
(a)

(b)

(c)

Figure 6: Time history of the transmittance on the FVM-P1 results: study of the influence of the time interval width Δt (Fig. (a)), the instant t_i (Fig. (b)) and of the buffer zone size Δd (Fig. (c)).
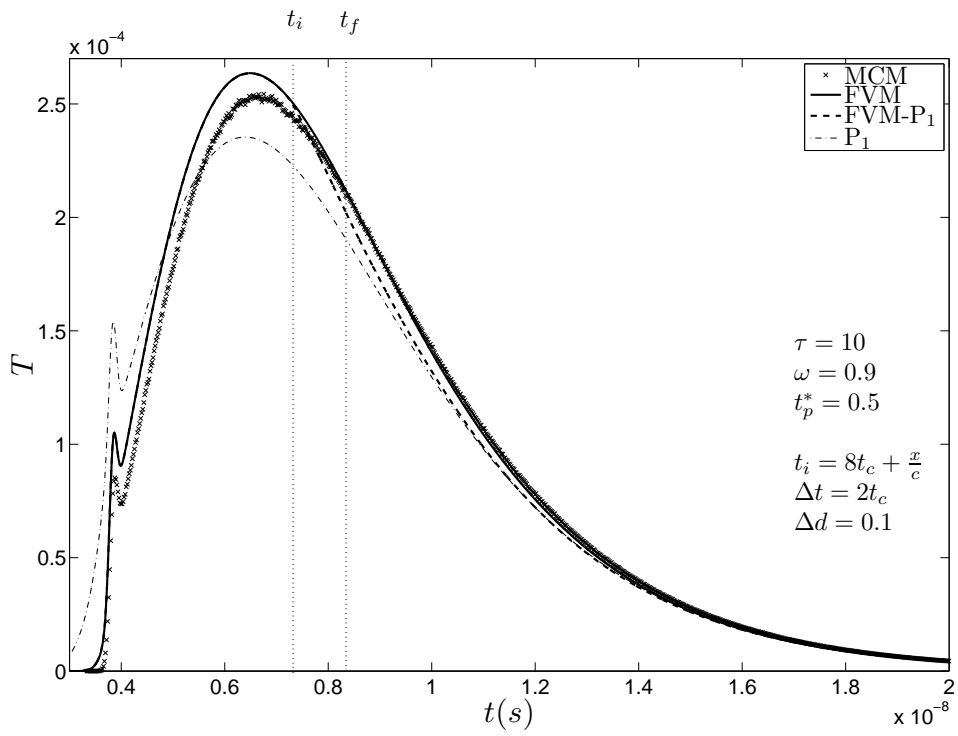
29

Figure 7: Time history of the transmittance: comparison between the Monte Carlo, FVM-P1, FVM, and P1 methods for an albedo equal to 0.9.